Advanced composites based on relaxor-ferroelectric single crystals: From electromechanical coupling to energy-harvesting applications

C. R. Bowen,[a] V. Yu. Topolov,[b] A. N. Isaeva,[b] and P. Bisegna[c]

Domain-engineered relaxor-ferroelectric single crystals with compositions near the morphotropic phase boundary are considered as a key component for modern high-performance piezo-active composites. The advantages of using the relaxor-ferroelectric single crystals of solid solutions of $(1 - x)Pb(Mg_{1/3}Nb_{2/3})O_3 - xPbTiO_3$ and $(1 - y)Pb(Zn_{1/3}Nb_{2/3})O_3 - yPbTiO_3$ in piezo-active composites of 2–2 and 1–3 configurations are discussed by taking into account the complex relationships between the outstanding properties of the components and the effective parameters of the composite structure as a whole. Examples of their high piezoelectric activity, strong electromechanical coupling, large piezoelectric anisotropy, and large hydrostatic parameters of the composites demonstrate how the relaxor-ferroelectric single-crystal component improves the effective parameters and promotes the formation of non-monotonic volume-fraction dependences of particular effective parameters that are of interest for a variety of piezotechnical applications, such as transducers, sensors, hydrophones, and energy-harvesting devices.

Introduction

Recent trends in research and manufacturing of piezoelectric transducers show that the new generation of relaxor-ferroelectric single crystals (RFSCs) with outstanding electromechanical properties[1–4] have a significant potential for the future development of piezo-active composites.[5–11] Such composites are regarded as high-performance smart materials with effective properties[9, 10] that can be tailored to a significant extent for particular applications. A study on the piezoelectric performance of piezo-active composites based on RFSCs requires a detailed knowledge and understanding of the interconnections between the electromechanical properties of the components and the particular features of the microgeometry of the composite[9–11] as a whole. Due to the considerable piezoelectric effect and high degree of electromechanical coupling in RFSCs,[1–4] the effective electromechanical transformation of energy is of interest for a variety of transducer applications and this also includes composites based on the RFSCs.[1, 3–7]

Piezoelectricity is a physical phenomenon that is concerned with the electromechanical coupling in dielectrics and is observed in acentric single crystals; the materials include ferroelectrics,[12-14] piezoelectric textures,[12, 13] poled ferroelectric ceramics,[14-16] piezoelectric paints,[17, 18] and composite structures.[9, 10, 19, 20] Research in the rapidly growing field of smart materials suggests that both ferroelectricity and piezoelectricity represent an important link between solid-state science and engineering and form an important stimulus for emerging piezotechnical and related applications.[2, 16, 20] Knowledge of the electromechanical properties of these materials and the potential to control their properties are the necessary conditions for the optimum use of RFSCs as advanced piezoelectric components of modern composites.[5-11] Moreover, variations in the microgeometry (connectivity) of composites based on RFSCs and the volume fraction, chemical composition, poling direction, and domain structure of the RFSC component lead to significant changes in the electromechanical properties of the composite.[3, 4, 9, 10] The aim of the present paper is to highlight the effective electromechanical properties and advantages of the RFSC-based composites for piezoelectric transducer and energy-harvesting applications.

Examples of domain-engineered relaxor-ferroelectric single crystals and their electromechanical properties

The overwhelming majority of relaxor-ferroelectric solid solutions studied for the past three decades are characterised by a perovskite-type structure.[1,2,14] Of particular interest are compositions that are described[2] by one of the following general formulae: $(1 - x)Pb(B_1, B_2)O_3 - xPbTiO_3$ or $(1 - x - y)Pb(B_1, B_2)O_3 - xPb(B_1', B_2')O_3 - yPbTiO_3$. In these formulae $Pb(B_1, B_2)O_3$ and $Pb(B_1', B_2')O_3$ are disordered perovskite-type compounds that contain ions of metals from the following groups: B_1 (or B_1') = Mg, Zn, Ni, Fe, Sc, Yb, and In (i.e., metals with low valence) and B_2 (or B_2') = Nb, Ta and W (i.e., metals with high valence). A combination of metal ions with low and high valences results in physical properties that distinguish $Pb(B_1, B_2)O_3$ from "normal" (ordered or regular) perovskite-type ferroelectrics[2, 14] such as $PbTiO_3$, $BaTiO_3$ or $KNbO_3$. The complex perovskites with the general formula $Pb(B_1, B_2)O_3$ exhibit a broad and frequency-dispersive dielectric maxima and contain polar nanoregions, that may have either ferro- or antiferroelectric ordering, in a non-polar phase over a wide temperature range. These materials are characterised by a relaxation dielectric polarisation and are termed *relaxors* or *ferroelectric relaxors*.[2]

The perovskite-type solid solutions of $(1 - x)Pb(B_1, B_2)O_3 - xPbTiO_3$ combine the physical properties of the relaxor-type and "normal" ferroelectric components and the best electromechanical properties are observed, as a rule, near the morphotropic phase boundary.[1-4] To achieve a high piezoelectric activity in RFSC samples, the relaxor-ferroelectric solid solutions are engineered by compositional adjustment and this leads to a corresponding decrease in the Curie temperature of the paraelectric-to-ferroelectric phase transition,[2] and specific domain-engineered structures are formed in the presence of an electric field.[1, 2, 21] A number of experimental studies have shown that there is significant interest in domain-engineered RFSCs of $(1 - x)Pb(Mg_{1/3}Nb_{2/3})O_3 - xPbTiO_3$ (PMN–*x*PT) and $(1 - y)Pb(Zn_{1/3}Nb_{2/3})O_3 - yPbTiO_3$ (PZN–*y*PT) (see, for instance, Refs. 1–4, 2 –24) with remarkable electromechanical properties that are related to their molar concentrations x in the vicinity of the morphotropic phase boundary. Other relaxor-ferroelectric solid solutions that are of particular interest for transducer applications include $(1 - x - y)Pb(In_{1/2}Nb_{1/2})O_3 - yPb(Mg_{1/3}Nb_{2/3})O_3 - xPbTiO_3$ [(1 – *x* – *y*)PIN – *y*PMN – *x*PT],[25, 26] $(1 - x - y)Pb(Yb_{1/2}Nb_{1/2})O_3 - yPb(Mg_{1/3}Nb_{2/3})O_3 - xPbTiO_3$ [(1 – *x* – *y*)PYN – *y*PMN – *x*PT],[27] and lead-free $(1 - x)(Na_{1/2}Bi_{1/2})TiO_3 - xBaTiO_3$ (NBT – *x*BT).[28]

The engineered non-180° domain structures,[21,22] intermediate ferroelectric phases[30-33] and domain-orientation processes[34] play a key role in the RFSCs that achieve outstanding electromechanical properties[25-28, 35-39] . The high piezoelectric activity in these RFSCs is often associated with a polarisation rotation[23] induced by an electric field ***E*** applied along a specific crystallographic direction. For example, the polarisation rotation between the single-domain states in the tetragonal (4*mm*) and rhombohedral (3*m*) phases of the ferroelectric nature can be implemented in different ways that form intermediate monoclinic phases and complex heterophase states.[23, 30, 31-33] Due to these, and other phenomena, the domain-engineered RFSCs that are poled along specific crystallographic directions (often along [001], [011], [101], or [111] of the perovskite unit cell, see, for instance, Fig. 1)[21, 25-29, 34, 40] exhibit the high piezoelectric activity and strong electromechanical coupling.

We now show examples of the room-temperature electromechanical properties of domain-engineered RFSCs (Tables 1 and 2) with compositions near the morphotropic phase boundary. It should be noted that the full set of electromechanical constants listed in Tables 1 and 2 originate from equations[12, 13]

$$\xi_p = S^E_{pq}\,\sigma_q + d_{fp}\,E_f \text{ and } D_k = d_{kl}\,\sigma_l + \varepsilon^{\sigma}_{kr}\,E_r \qquad (1)$$

which describe the electroelastic behaviour of a piezoelectric medium. In Eqs. (1), ξ_p is a mechanical strain as a result of an external mechanical stress σ_q and electric field E_f, D_k is an electric displacement due to the same stress and electric field, S^E_{pq} is elastic compliance measured at E = const, d_{fp} is piezoelectric coefficient, and $\varepsilon^{\sigma}_{kr}$ is dielectric permittivity measured at σ = const. In Eqs. (1), the matrix representation of the electromechanical properties and field components is used.[9, 10, 12, 13] The piezoelectric properties play an important role in forming the electromechanical coupling and energy conversion. As is known, there are four pairs of equations that can be used to describe[9, 10, 12, 13] the electromechanical properties such as those in Eqs. (1). The piezoelectric coefficients of

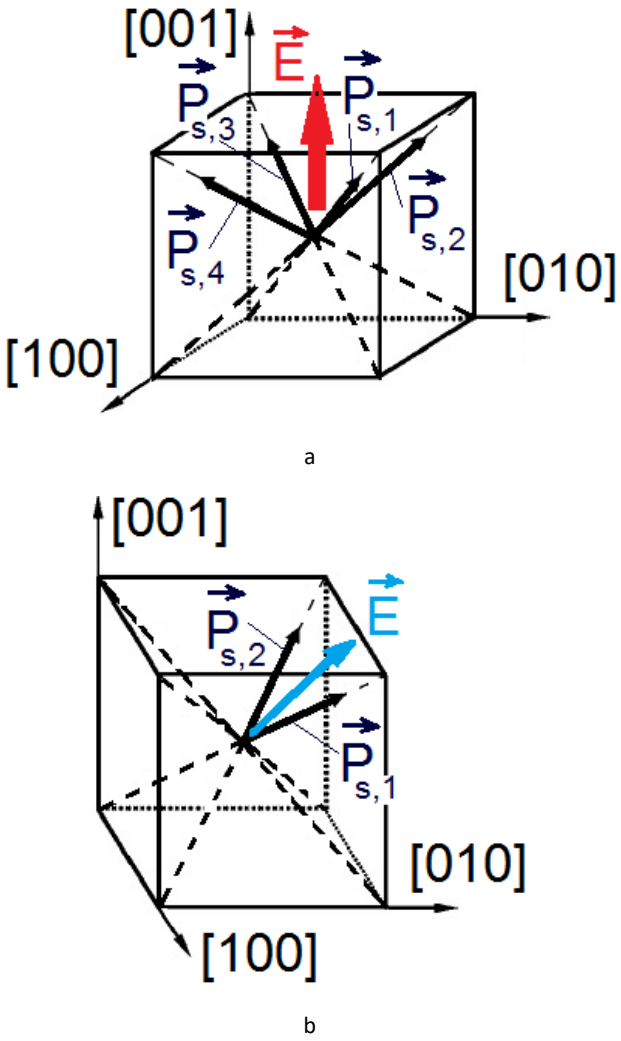

Fig. 1. Schematic arrangement of non-180° domains in the [001]-poled (a) and [011]-poled (b) single crystal samples. $\boldsymbol{P_{s,1}}$, $\boldsymbol{P_{s,2}}$, $\boldsymbol{P_{s,3}}$, and $\boldsymbol{P_{s,4}}$ are spontaneous polarisation vectors of several domain types, ***E*** is the poling direction, and [100], [010] and [001] are perovskite unit-cell directions.

the piezoelectric medium are divided[9, 10, 12, 13] into four groups, namely, d_{ij}, e_{fp}, g_{ij}, and h_{ij}, and are to be considered in the context of specific links between the electric and mechanical fields as a result of the direct or converse piezoelectric effect.

Of particular interest are piezoelectric coefficients d_{ij} that link[12, 13] the polarisation of a material and a mechanical stress applied to it. Typical values of $|\,d_{3j}\,|$ are $\sim 10^3$ pC / N in the domain-engineered RFSCs poled along either the [001] axis (see Fig. 1a and Table 1) or the [011] axis (see Fig. 1b and Table 2) in the perovskite unit cell. Such values are larger than, for instance, the $|\,d_{3j}\,|$ values of the regular ferroelectric single-domain $PbTiO_3$ single crystal[41] or poled ferroelectric ceramics based on $Pb(Zr_{1-x}Ti_x)O_3$.[14–16] It is seen that the change in the poling direction leads to a change in the anisotropy of the properties, e.g., the anisotropy of the piezoelectric coefficients d_{3j} (cf. d_{3j} of the same RFSCs from Tables 1 and 2). It is known from experimental room-temperature data,[25, 26, 35, 36] that the RFSCs shown in Table 1 are characterised by

3*m* symmetry in the single-domain state and by 4*mm* symmetry in the polydomain (domain-engineered) state where the spontaneous polarisation vectors of the ferroelectric non-180° domains are parallel to the [111], [$\bar{1}$11], [1$\bar{1}$1], and [$\bar{1}\bar{1}$1] directions of the perovskite unit cell (Fig. 1a).The RFSCs shown in Table 2 are characterised by 3*m* symmetry in the single-domain state, but by *mm*2 symmetry in the polydomain (domain-engineered) state which is concerned with two domain types (Fig. 1b). It should be added that in some cases the reported full sets of electromechanical constants measured on RFSC are inconsistent in terms of the piezoelectric coefficients of the four groups (d_{ij}, e_{fp}, g_{ij}, and h_{ij}) and this has been discussed in Ref. 47.

The outstanding electromechanical properties of the domain-engineered RFSCs (Tables 1 and 2) and large absolute values of their electromechanical coupling factors[3, 4, 9, 10]. enable us to consider these materials as active components of advanced piezo-active composites that may be suitable for sensors, actuators, highly sensitive medical ultrasonic transducers, hydrophones, ultrasonic imaging devices, and energy-harvesting devices. In the sections below we will highlight and discuss examples and advantages of using the domain-engineered RFSCs in high-performance composites. In addition, we will analyse the role of the RFSC component in forming a large anisotropy of the piezoelectric properties and high electromechanical coupling factors in composite systems.

2–2-type composites and their performance

The composite with 2–2 connectivity (in terms of classification proposed by Newnham et al.[48]) represents a system of layers of two components (see, for instance, the schematic in Fig. 2). The family of the 2–2 piezo-active composites comprises examples of the ferroelectric ceramic / polymer[9, 10, 20] and RFSC / polymer[3, 4, 9, 10] composites. They are characterised by laminar structures with a regular or irregular distribution of components,[9, 10, 20] with different poling directions and orientations of the interfaces with respect to the poling direction[49-51] etc. According to work,[52] the 2–2 connectivity pattern is one of the so-called junction connectivity patterns in two-component composites with planar interfaces that separate each component. Combinations and/or multiplications of the junction connectivity patterns lead to other connectivity patterns of the two-component composites. The relatively simple laminar structure of the 2–2-type composite and properties it make this composite attractive for a variety of transducer applications. Now we discuss some examples of the high performance of the 2–2-type composite based on RFSC.

2–2 composite based on PZN–0.07PT

The full sets of electromechanical constants have initially been measured on domain-engineered PZN–0.07PT RFSC samples are poled[36, 38] in either the [001] or [011] direction in the perovskite axes. The symmetry and anisotropy of the electromechanical properties of the [011]-poled RFSC differ from the properties of the [001]-poled RFSC with the same chemical composition (see, for instance, data on PMN–0.28PT, PMN–0.29PT and PZN–0.07PT in Tables 1 and 2).

We highlight an example of a 2–2 composite based on the [011]-poled PZN–0.07PT RFSC. It is assumed that the parallel-connected layers (either RFSC or polymer) are continuous in the OX_2 and OX_3 directions and alternating in the OX_1 direction (Fig. 2). The main crystallographic axes X, Y and Z in each RFSC layer are parallel to the following perovskite unit-cell directions: X || [0$\bar{1}$1], Y || [100] and Z || [011]. In all the RFSC layers of the composite system, the main crystallographic axes X and Y rotate around the co-ordinate axis OX_3 clockwise by the angle φ. At φ = 0, the conditions X || OX_1, Y || OX_2 and Z || OX_3 hold. The composite sample is poled along the OX_3 axis, and the poling direction does not depend on φ (Fig. 2).

Table 1. Elastic compliances s_{ab}^E (in 10^{-12} Pa^{-1}), piezoelectric coefficients d_{ij} (in pC / N) and dielectric permittivities $\varepsilon_{pp}^{\sigma}$ of [001]-poled domain-engineered RFSCs (4*mm* symmetry) at room temperature

RFSCs	s_{11}^E	s_{12}^E	s_{13}^E	s_{33}^E	s_{44}^E	s_{66}^E	d_{31}	d_{33}	d_{15}	$\varepsilon_{11}^{\sigma}/\varepsilon_0$	$\varepsilon_{33}^{\sigma}/\varepsilon_0$
PMN–0.33PT, Ref. 35	69.0	–11.1	–55.7	119.6	14.5	15.2	–1330	2820	146	1600	8200
PMN–0.30PT, Ref. 42	52.0	–18.9	–31.1	67.7	14.0	15.2	–921	1981	190	3600	7800
PMN–0.29PT, Ref. 43	52.1	–24.6	–26.4	59.9	16.0	28.3	–699	1540	164	5400	1560
PMN–0.28PT, Ref. 44	44.57	–28.91	–13.91	34.38	15.22	16.34	–569	1182	122	1672	5479
PZN–0.045PT, Ref. 39	82.0	–28.5	–51.0	108	15.6	15.9	–970	2000	140	3100	5200
PZN–0.07PT, Ref. 36	85.9	–14.1	–69.0	142	15.9	14.1	–1204	2455	176	3000	5622
PZN–0.08PT, Ref. 36	87.0	–13.1	–70.0	141	15.8	15.4	–1455	2890	158	2900	7700
0.26PIN – 0.42PMN – 0.32PT:Mn,[a] Ref. 25	45.4	–15.9	–28.1	62.4	15.4	27.8	–609	1341	133	1326	3811
0.27PIN– 0.40PMN– 0.33PT, Ref. 26	75.5	–38.3	–35.8	77.8	14.5	16.1	–1337	2742	232	10081	7244
NBT–0.05BT, Ref. 28	12.2	–3.4	–8.2	27.7	13.4	12.9	–113	360	162	1099	1021

[a] Level of doping Mn is from 1 to 5 mol. %

Table 2. Elastic compliances s_{ab}^{E} (in 10^{-12} Pa^{-1}), piezoelectric coefficients d_{ij} (in pC / N) and dielectric permittivities $\varepsilon_{pp}^{\sigma}$ of [011]-poled domain-engineered RFSCs (*mm*2 symmetry) at room temperature

Electromechanical constants	PMN–0.28PT, Ref. 44	PMN–0.29PT, Ref. 45	PZN–0.07PT, Ref. 38	PZN–0.09PT, Ref. 46	0.26PIN–0.42PMN–0.32PT:Mn,[a] composition A, Ref. 25	0.26PIN–0.42PMN–0.32PT:Mn,[a] composition B, Ref. 25
s_{11}^{E}	13.40	18.0	67.52	73.07	18.0	23.5
s_{12}^{E}	–21.18	–31.1	–60.16	–63.98	–28.0	–39.0
s_{13}^{E}	–12.67	8.4	3.355	4.256	13.1	20.6
s_{22}^{E}	54.36	11.2	102.0	125.6	68.1	90.4
s_{23}^{E}	–39.59	–61.9	–54.47	–68.04	–39.4	–56.4
s_{33}^{E}	28.02	49.6	62.02	67.49	30.9	43.8
s_{44}^{E}	15.22	14.9	15.45	15.12	15.5	16.2
s_{55}^{E}	147.06	69.4	291.5	299.3	116	189
s_{66}^{E}	22.47	13.0	14.08	16.54	20.0	21.1
d_{15}	2162	1188	1823	2012	2030	2986
d_{24}	160	167	50	118.7	125	160
d_{31}	447	610	478	476.0	455	608
d_{32}	–1150	–1883	–1460	–1705	–1200	–1508
d_{33}	860	1030	1150	1237	810	1053
$\varepsilon_{11}^{\sigma} / \varepsilon_0$	4235	3564	8240	8740	4916	6274
$\varepsilon_{22}^{\sigma} / \varepsilon_0$	1081	1127	1865	2075	1084	1499
$\varepsilon_{33}^{\sigma} / \varepsilon_0$	3873	4033	3180	3202	3213	3523

[a] Level of doping Mn is from 1 to 5 mol. %

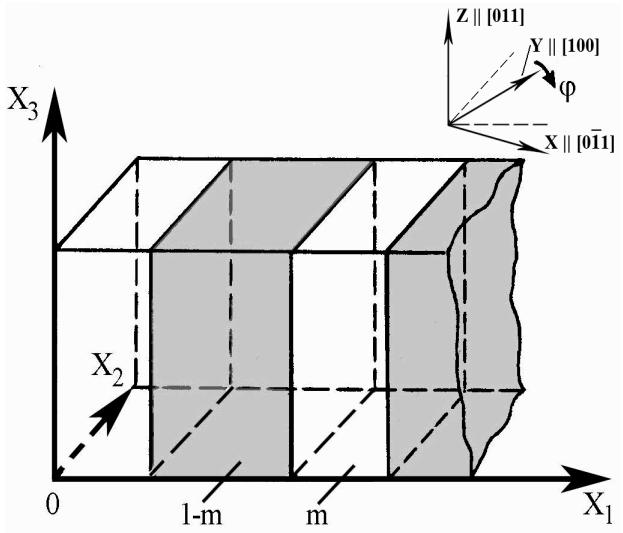

Fig. 2. Schematic of the 2–2-type composite with parallel-connected layers. ($X_1X_2X_3$) is the rectangular co-ordinate system. *m* and 1 – *m* are volume fractions of the RFSC and polymer components, respectively, and φ is the angle of rotation of the main crystallographic axes *X* and *Y* of around the OX_3 axis that is parallel to *Z* (reprinted from Krivoruchko and Topolov,[49] with permission from IOP Publishing, www.iop.org).

The determination of the effective electromechanical properties of the 2–2 RFSC / polymer composite is performed within the framework of the matrix method[9, 10] by taking into account the nine boundary conditions at x_1 = const. These boundary conditions require the continuity of three normal components of the mechanical stress (σ_{11}, σ_{12} and σ_{13}), three tangential components of the mechanical strain (ξ_{22}, ξ_{23} and ξ_{33}), one normal component of the electric displacement (D_1), and two tangential components of the electric field (E_2 and E_3). The effective electromechanical properties of the 2–2 composite are represented in the matrix form[10] as follows:

$$|| C^* || = [|| C^{(1)} ||\cdot|| M || m + || C^{(2)} || (1 - m)][|| M || m + || I || (1 - m)]^{-1}. \quad (2)$$

In Eq. (2), $|| C^{(1)} ||$ and $|| C^{(2)} ||$ are the matrices of electromechanical constants of the RFSC [superscript (1)] and polymer [superscript (2)] components, $|| I ||$ is the identity matrix, $|| M ||$ is the matrix that is concerned with the aforementioned boundary conditions, and *m* is the volume fraction of the RFSC component. The $|| C^{(n)} ||$ matrices are given by

$$|| C^{(n)} || = \begin{pmatrix} || s^{(n),E} || & || d^{(n)} ||^t \\ || d^{(n)} || & || \varepsilon^{(n),\sigma} || \end{pmatrix}, \quad (3)$$

where $|| s^{(n),E} ||$ is the 6×6 matrix of elastic compliances at E = const, $|| d^{(n)} ||$ is the 3×6 matrix of piezoelectric coefficients and $|| \varepsilon^{(n),\sigma} ||$ is the 3×3 matrix of dielectric permittivities σ = const of the RFSC (n = 1) and polymer (n = 2) components, and superscript *t* denotes the transposition. The $|| C^* ||$ matrix from Eq. (2) has the form similar to that shown in Eq. (3). The effective electromechanical properties of the 2–2 composite, i.e., full sets of $s_{ab}^{*E}(m, \varphi)$, $d_{ik}^{*}(m, \varphi)$ and $\varepsilon_{pp}^{*\sigma}(m, \varphi)$, are determined within the framework of the longwave approximation.[9, 10] This approximation means that the wavelength of acoustic waves propagated is

considerably longer than the thickness of each layer (Fig. 2) in the composite structure. Based on elements of || $C^*(m, \varphi)$ || from Eq. (2), we evaluate the effective piezoelectric coefficients g_{ik}^*, the hydrostatic piezoelectric coefficients

$$d_h^* = d_{33}^* + d_{32}^* + d_{31}^* \quad (4)$$

and

$$g_h^* = g_{33}^* + g_{32}^* + g_{31}^* = d_h^* / \varepsilon_{33}^{*\sigma}, \quad (5)$$

squared figures of merit

$$(Q_{3j}^*)^2 = d_{3j}^* g_{3j}^* = (d_{3j}^*)^2 / \varepsilon_{33}^{*\sigma} \quad (6)$$

and

$$(Q_h^*)^2 = d_h^* g_h^* = (d_h^*)^2 / \varepsilon_{33}^{*\sigma}, \quad (7)$$

and electromechanical coupling factors

$$k_{3j}^* = d_{3j}^* (s_{jj}^{*E} \varepsilon_{33}^{*\sigma})^{-1} \quad (8)$$

and

$$k_h^* = d_h^* (s_h^{*E} \varepsilon_{33}^{*\sigma})^{-1} \quad (9)$$

of the 2–2 composite, where j = 1, 2 and 3, and $s_h^{*E} = s_{11}^{*E} + s_{22}^{*E} + s_{33}^{*E} + 2(s_{12}^{*E} + s_{13}^{*E} + s_{23}^{*E})$ is the hydrostatic elastic compliance at E = const. The piezoelectric coefficients from Eqs. (4) and (5) are used for description of the hydrostatic activity and sensitivity, respectively. The squared figures of merit from Eqs. (6) and (7) are introduced to describe the sensor signal-to-noise ratio of the piezoelectric element.[9, 10, 53] The electromechanical coupling factors from Eqs. (8) and (9) are used to characterise effectiveness of the conversion of mechanical energy into electric energy and vice versa.[9, 10, 12, 13] It should be added that Eqs. (4)–(8) are related to the composite sample with electrodes oriented parallel to the (X_1OX_2) plane (see Fig. 2). Our evaluations of the effective properties and related parameters of the piezo-active composites are carried out by using experimental data on components (Tables 1–3).

The high piezoelectric activity of the studied 2–2 composite even at relatively small volume fractions of RFSC 0.05 < m < 0.10 (curves 1–4 in Fig. 3a) leads to a high piezoelectric sensitivity (curves 5–8 in Fig. 3a). This is due to the large piezoelectric coefficient $d_{33}^{(1)}$ of the RFSC layer (see Table 2) and a relatively slow increase of the effective dielectric permittivity of the composite $\varepsilon_{33}^{*\sigma}$ with increasing m. The hydrostatic piezoelectric coefficient g_h^* is larger than $g_h^{(1)}$ = 5.97 mV·m / N of the [011]-poled PZN–0.07PT RFSC, and in ranges 0.05 < m < 0.10 and 45° < φ < 90° (Fig. 3a) the condition $g_h^* / g_h^{(1)} > 10$ is valid. The squared hydrostatic figure of merit and $(Q_h^*)^2$ from the aforementioned m and φ ranges (Fig. 3b) is approximately 5–30 times larger than $(Q_h^{(1)})^2 = 1.00 \cdot 10^{-12}$ Pa^{-1} of the [011]-poled PZN–0.07PT RFSC. This performance is achieved due to the combination of the high piezoelectric activity and sensitivity of the composite. The orientation of the main crystallographic axes at φ = 90° leads to the largest value of $(Q_h^*)^2$ of the composite for m = const: at such an orientation the influence of the piezoelectric coefficient $d_{32}^{(1)} < 0$ on the piezoelectric coefficients d_h^* and g_h^* from Eqs. (4) and (5) becomes minimal. The values of $(Q_h^*)^2$ at 60° ≤ φ ≤ 90° and 0.05 < m < 0.15 (see curves 2–4 in Fig. 3b) are larger than max[$(Q_h^*)^2$] = $1.4 \cdot 10^{-11}$ Pa^{-1} of a 2–2 oriented PZT ceramic/polymer composite[20] and 2–2 conventional ferroelectric ceramic/polymer composites.[9, 10, 58]

Table 3. Experimental values of elastic compliances s_{ab} (in 10^{-12} Pa^{-1}) and dielectric permittivities ε_{pp} of polymers at room temperature

Polymers	s_{11}	s_{12}	$\varepsilon_{pp} / \varepsilon_0$
Araldite[54]	216	–78	4.0
Polyurethane[55]	401	–151	3.5
Elastomer[53]	3300	–1480	5.0
Polyethylene (high-density)[56]	1540	–517	2.3[a]
Auxetic polyethylene[56]	5290	4400	2.3[a]

[a] Dielectric permittivity of monolithic polyethylene, Ref. 57

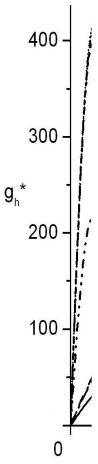

Table 4. Absolute maxima of hydrostatic piezoelectric coefficients d_h^* (in pC / N) of the 2–2 PMN–xPT RFSC / auxetic polyethylene composite[59] at rotation modes shown in insets 3–5 in Fig. 4

RFSC poling direction	x	Absolute max d_h^*	
		Value	Corresponding rotation angle and volume fraction of RFSC
[001]	0.28	939	α = 0°, m = 0.029
	0.30	1210	α = 0°, m = 0.101
	0.33	1410	α = 0°, m = 0.177
[011]	0.28	1650	γ = 0°, m = 0.074
	0.29	1990	γ = 0°, m = 0.072

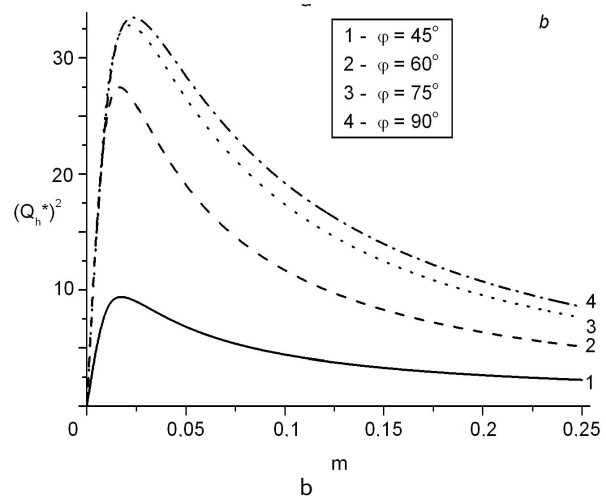

Fig. 3. Effective parameters of the 2–2 PZN–0.07PT RFSC / elastomer composite: (a) hydrostatic piezoelectric coefficients d_h^* (in pC / N) and g_h^* (in mV m / N) and (b) squared hydrostatic figure of merit $(Q_h^*)^2$ (in 10^{-12} Pa^{-1}). The RFSC layers of the composite sample shown in Fig. 2 are poled along [011] of the perovskite unit cell (reprinted from Krivoruchko and Topolov,[49] with permission from IOP Publishing, www.iop.org).

2-2-type composites based on PMN–*x*PT

Now we compare some effective parameters related to the 2–2-type composites based on the PMN–xPT RFSC. It is assumed that the RFSC layers are poled along either the [001] (inset 1 in Fig.

4) or [011] direction of the perovskite unit cell (inset 2 in Fig. 4). We consider the rotation of the main crystallographic axes X, Y and Z of the polydomain RFSC layer around one of the co-ordinate axes as follows: OX_1 || X (inset 3 in Fig. 4), OX_2 || Y (inset 4 in Fig. 4) or OX_3 || Z (inset 5 in Fig. 4). These rotation modes enable us to maintain polydomain states in the RFSC layers and to study the polarisation orientation effect. It is assumed that at these rotation modes, the spontaneous polarisation vectors of domains $\boldsymbol{P_{s,1}}$, $\boldsymbol{P_{s,2}}$ etc. in each RFSC layer are situated either over or in the (X_1OX_2) plane (see Fig. 4). The rotation angles α, β and γ can then be changed[10, 59] as follows:

(i) $-45° \le \alpha \le 45°$ or $-45° \le \beta \le 45°$ (composite based on the [001]-poled RFSC, see rotation modes in insets 3 and 4 in Fig. 4) and

(ii) $-\arcsin(1/\sqrt{3}) \le \alpha \le \arcsin(1/\sqrt{3})$, $-45° \le \beta \le 45°$ or $0° \le \gamma \le 360°$ (composite based on the [011]-poled RFSC, see rotation modes in insets 3–5 in Fig. 4).

As a result of the 4*mm* symmetry of the [001]-poled polydomain RFSC (see Table 1 and inset 1 in Fig. 4) and $d_{31}^{(1)} = d_{32}^{(1)}$ for this symmetry class, we do not consider the rotation of the main crystallographic axes around OX_3 || Z in case (i). Among the polymer components of interest, we choose an auxetic polyethylene with a Poisson's ratio that equals –0.83 (see data in Table 3). The ratio between the elastic compliances $s_{11}^{(2)}$ and $s_{12}^{(2)}$ of the auxetic polymer component strongly influences the piezoelectric properties and electromechanical coupling of the composite, especially at relatively small volume fractions *m*. In this study we do not take into consideration the specifics of the microgeometry of the auxetic polyethylene,[56] and therefore, the composite is regarded as a 2–2-type composite. The effective electromechanical properties are evaluated by means of the matrix method.[10, 59]

The largest value of absolute max d_h^* in the composite based on the [001]-poled RFSC (Table 4) is achieved in samples with PMN–0.33PT layers that are charactersised by the largest value of $d_h^{(1)}$. The largest value of absolute max d_h^* is achieved in the composite based on the [011]-poled RFSC with the largest value of $|d_h^{(1)}|$ (i.e., at *x* = 0.29). The absolute maxima of $(Q_h^*)^2$ and $(Q_{3j}^*)^2$ in the studied composite are achieved at small volume fractions of RFSC ($0 < m < 0.02$) irrespective of *x* and poling direction, and it would be difficult to manufacture the requested composite samples within this particular volume-fraction range. The volume-fraction behaviour of $(Q_h^*)^2$ and $(Q_{33}^*)^2$ shows that their decrease is due to an increase of $\varepsilon_{33}^{*\sigma}$ on increasing *m*. The important feature of the studied composite is the fact that the condition

$$(Q_{33}^*)^2 / (Q_{3j}^*)^2 \ge 10 \ (j = 1 \text{ and } 2) \qquad (10)$$

holds within a wide range of the volume fractions *m* and rotation angles, in the presence of the RFSC component poled either along [001] (Fig. 5a) or [011] (Fig. 5b) and at different rotation modes. It should be added that a considerable part of the hatched area in Fig. 5a is related to (m, α) that provides a large value of local max[$(Q_h^*)^2$]. This performance is due to the orientation effect and elastic anisotropy in the studied composite and the relatively high piezoelectric activity of its RFSC component. It should be noted that for to the [001]-poled PMN–0.33PT RFSC, according to data from Table 1, the relation $(Q_{33}^{(1)})^2 / (Q_{31}^{(1)})^2 = (Q_{33}^{(1)})^2 / (Q_{32}^{(1)})^2 = (d_{33}^{(1)} / d_{31}^{(1)})^2 \approx$ 4.5 is valid, i.e., the piezoelectric anisotropy of this RFSC is not large. In contrast to this, Eq. (10) and Fig. 5 show advantages of the studied 2–2-type composite wherein the auxetic polyethylene leads to the larger anisotropy of the piezoelectric coefficients d_{3f}^* and squared figures of merit $(Q_{3f}^*)^2$. Such a performance of the composite is important for piezoelectric transducer, actuator and energy-harvesting applications.

1–3-type composites and their performance

The study of 1–3 RFSC / polymer composites (Fig. 6) has been widespread in the last decade.[5-10] In such a composite structure, the RFSC component is self-connected in one dimension, and the polymer component is self-connected in three dimensions. The 1–3 composite sample consists of a system of the long aligned piezoelectrics (single-crystal or ceramic) rods surrounded by a large polymer matrix, and the matrix can be either piezoelectric or piezo-passive. Examples of the application of the RFSC as a highly effective component in the advanced 1–3 composite and its piezoelectric performance are discussed in Refs. 3–10. The growth of high-quality RFSCs and the formation of engineered domain structures within them are important for creating novel high-performance piezo-active composites. A modification of properties of the polymer matrix surrounding the RFSC rods in the 1–3-type composite leads to a further improvement in its performance such as the piezoelectric sensitivity, figures of merit and electromechanical coupling.[60-64] In the present section we highlight examples of the effective parameters of the 1–3-type composites based on the aforementioned RFSCs.

Maxima of effective parameters of 1–3 composites

It is assumed that the 1–3 composite contains a system of RFSC rods in the form of rectangular parallelepipeds with the square base (Fig. 6). These parallelepipeds are continuous in the OX_3 direction, and their lateral faces are parallel to the (X_1OX_3) and (X_2OX_3) planes. In a case of the [001]-poled RFSC component, its main crystallographic axes X, Y and Z are oriented as follows: X || OX_1, Y || OX_2 and Z || OX_3, and OX_3 is regarded as a poling axis for the

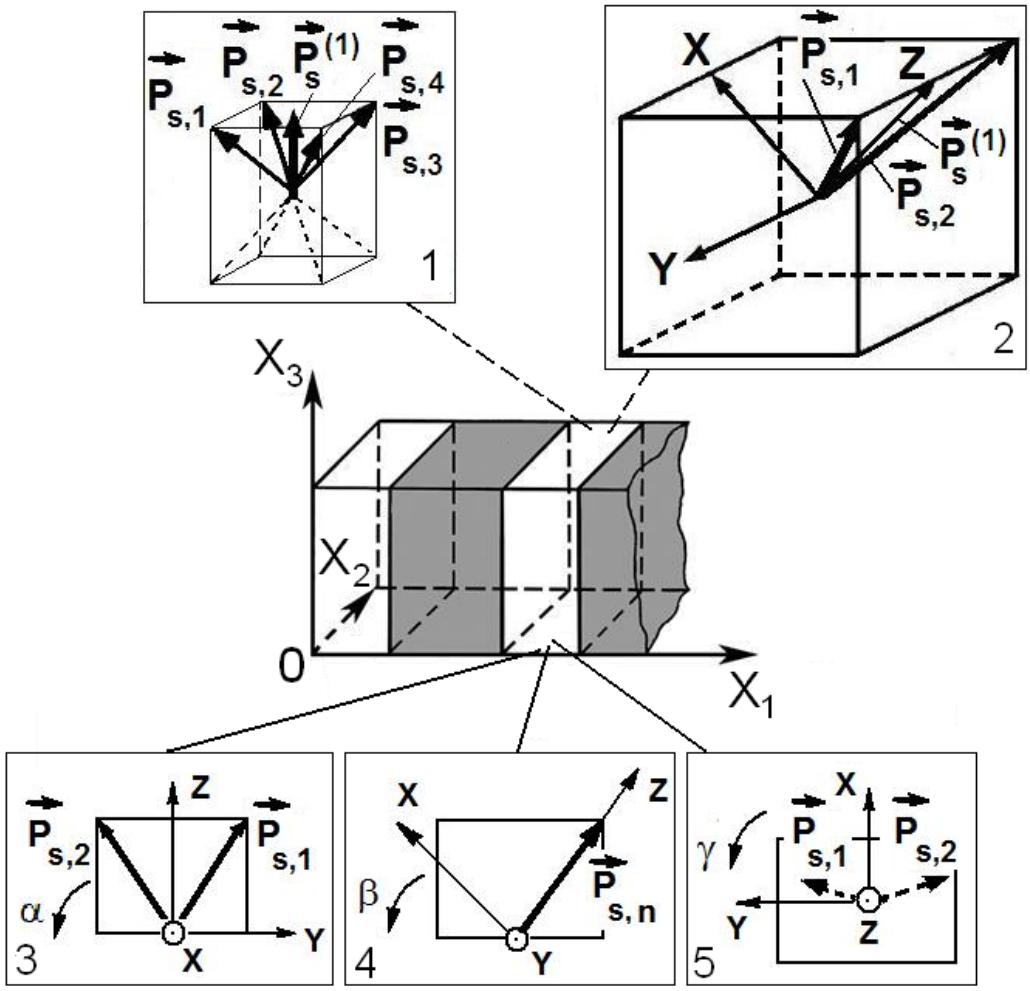

Fig. 4. Schematic of the 2–2 RFSC / polymer composite with parallel-connected layers. ($X_1X_2X_3$) is a rectangular co-ordinate system. Inset 1 comprises domain orientations in the [001]-poled RFSC layer with the effective spontaneous polarisation vector $\boldsymbol{P}_s^{(1)}$. Inset 2 comprises domain orientations in the [011]-poled RFSC layer with the effective spontaneous polarisation vector $\boldsymbol{P}_s^{(1)}$. $\boldsymbol{P}_{s,1}$, $\boldsymbol{P}_{s,2}$, $\boldsymbol{P}_{s,3}$, and $\boldsymbol{P}_{s,4}$ are spontaneous polarisation vectors of several domain types, and X, Y and Z are the main crystallographic axes in each RFSC layer. In inset 1, X, Y and Z are parallel to the co-ordinate axes OX_1, OX_2 and OX_3, respectively. α, β and γ are angles of rotation of the main crystallographic axes and spontaneous polarisation vectors $\boldsymbol{P}_{s,n}$ around one of the co-ordinate axes OX_j (insets 3–5) (reprinted from Bowen and Topolov,[59] with permission from Taylor and Francis, http://taylorandfrancis.com).

composite sample as a whole. The rods are regularly distributed in the polymer matrix so that centres of symmetry of the rod bases form a simple square lattice in the (X_1OX_2) plane. The electrodes are parallel to the (X_1OX_2) plane. The effective electromechanical properties of the 1–3 composite are determined by means of the matrix method,[9, 10, 60] and boundary conditions are applied to interfaces x_1 = const and x_2 = const (see Fig. 6).

The 1–3 PMN–0.33PT / araldite composite is characterised by the largest maximum values of the parameters listed in Table 5: for instance, $\max d_h^*(m) = 1.71\, d_h^{(1)}$, $\max[Q_{33}^*(m)]^2 = 1.31(Q_{33}^{(1)})^2$ and $\max[Q_h^*(m)]^2 = 21.1(Q_h^{(1)})^2$. This is mainly due to the large values of $|d_{3f}^{(1)}|$ and $|s_{ab}^{(1),E}|$ of the RFSC component poled along [001] (see data in Table 1). As with the 2–2-type composites, maxima of g_{33}^* and g_h^* of the 1–3 composites are related to small volume fractions *m;* this is related to a significant increase in d_{32}^* and $|d_{31}^*|$ and a slow increase of $\varepsilon_{33}^{*\sigma}$ at $m << 1$. The columnar structure of the 1–3 composite leads to large values of d_h^*, $(Q_{33}^*)^2$ and $(Q_h^*)^2$ at larger volume fractions, $m \geq 0.1$ (Table 5), irrespective of the RSFC component making the 1–3 composite of interest for sensor, energy-harvesting and hydroacoustic applications.

It is of interest to note that the maximum values of the parameters of 1–3 composites based on PZN–0.07PT and PZN–0.08PT (Table 5) differ by only a few percent. However a simple comparison of the electromechanical constants of these RFSCs from Table 1 indicates the distinct differences in the hydrostatic piezoelectric response: e.g., $d_h^{(1)}$ = 47 pC / N and $g_h^{(1)}$ = 0.945 mV·m / N for PZN–0.07PT, and $d_h^{(1)}$ = –20 pC / N and $g_h^{(1)}$ = –0.293 mV·m / N for PZN–0.08PT. The high performance of the 1–3 composites is a result of the electromechanical interaction between the highly piezo-active rods in the composite structure and the polymer matrix

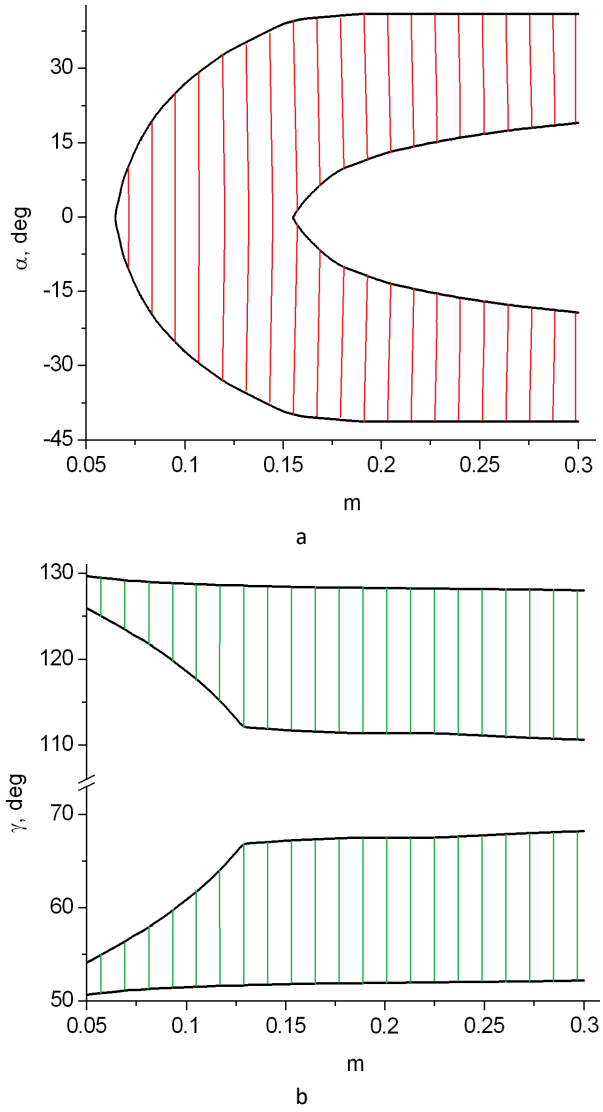

Fig. 5. Regions of validity of condition (10) (hatched areas in graphs) at different rotation modes in 2–2-type PMN–*x*PT RFSC / auxetic polyethylene composites: (a) composite based on the [001]-poled RFSC at *x* = 0.33 and (b) composite based on the [011]-poled RFSC at *x* = 0.29 (reprinted from Bowen and Topolov,[59] with permission from Taylor and Francis, http://taylorandfrancis.com).

surrounding the rods playing a passive role in this interaction. As a consequence, large values of specific parameters for the 1–3 composites[9, 60] can be achieved in a wide volume-fraction range. For instance, max d_h^* is achieved at a volume fraction *m* that is about 20–30 times larger than *m* related to max g_h^* (Table 5). We also note that max$[Q_{33}^*(m)]^2$ / max$[Q_h^*(m)]^2 \approx 25$ is the highest value for the composites listed in Table 5, and this value is achieved with PZN–0.08PT RFSC despite its negative piezoelectric coefficient $d_h^{(1)} = -20$ pC / N.

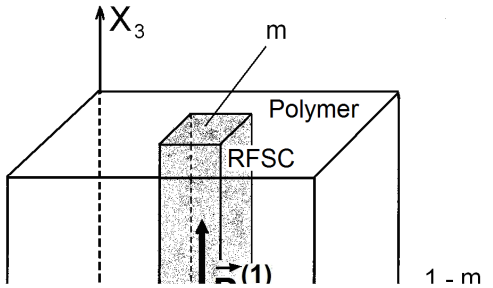

Table 5. Maximum values of piezoelectric coefficients g_{33}^* (in mV·m / N), d_h^* (in pC / N) and g_h^* (in mV m / N), and squared figures of merit $(Q_{33}^*)^2$ (in 10^{-12} Pa^{-1}) and $(Q_h^*)^2$ (in 10^{-12} Pa^{-1}) of the 1–3 [001]-poled RFSC / araldite composite[60]

RFSCs	max g_{33}^*	max d_h^*	max g_h^*	max[$(Q_{33}^*)^2$]	max[$(Q_h^*)^2$]
PMN–0.30PT	382 (0.013)[a]	244 (0.434)	103 (0.013)	106 (0.160)	6.16 (0.099
PMN–0.33PT	496 (0.017)	274 (0.509)	130 (0.016)	144 (0.250)	7.45 (0.115
PZN–0.045PT	317 (0.021)	180 (0.438)	81.0 (0.019)	108 (0.338)	4.62 (0.141
PZN–0.07PT	359 (0.023)	194 (0.455)	93.9 (0.021)	133 (0.460)	5.43 (0.146
PZN–0.08PT	352 (0.019)	206 (0.409)	90.6 (0.018)	136 (0.422)	5.38 (0.131

Table 5. Maximum values of piezoelectric coefficients g_{33}^* (in mV·m / N), d_h^* (in pC / N) and g_h^* (in mV m / N), and squared figures of merit $(Q_{33}^*)^2$ (in 10^{-12} Pa^{-1}) and $(Q_h^*)^2$ (in 10^{-12} Pa^{-1}) of the 1–3 [001]-poled RFSC / araldite composite[60]

RFSCs	max g_{33}^*	max d_h^*	max g_h^*	max$[(Q_{33}^*)^2]$
PMN–0.30PT	382 (0.013)[a]	244 (0.434)	103 (0.013)	106 (0.160)
PMN–0.33PT	496 (0.017)	274 (0.509)	130 (0.016)	144 (0.250)
PZN–0.045PT	317 (0.021)	180 (0.438)	81.0 (0.019)	108 (0.338)
PZN–0.07PT	359 (0.023)	194 (0.455)	93.9 (0.021)	133 (0.460)
PZN–0.08PT	352 (0.019)	206 (0.409)	90.6 (0.018)	136 (0.422)

[a] The volume fraction *m* at which maximum of the effective parameter is achieved

Piezoelectric performance of 1–3-type composites with auxetic polymer matrices

An increase in the effective parameters can be attained by a change in the elastic properties of the matrix in the 1–3 composite. The monolithic polymer matrix surrounding the RFSC rods can be replaced by either an auxetic polymer matrix[65] or a porous polymer matrix.[60,61] Now we discuss a performance of the 1–3-type composites (Fig. 6) that consist of the RFSC rods and an auxetic polymer matrix. The rods with square bases are characterised by a regular arrangement, and the centres of symmetry of these rods

form a simple square lattice in the (X_1OX_2) plane. To evaluate the effective parameters of the composites, we apply the matrix method.[10, 60]

We compare data obtained by means of the matrix method[10] to results of finite element modeling (FEM).[10] Here, the COMSOL package[66] is applied to obtain the volume-fraction dependence of the effective electromechanical properties of the composite within the FEM framework. In particular, a square unit cell, obtained by intersecting the rectangular parallelepiped with the (X_1OX_2) plane (see the schematic in Fig. 6) is adjusted to yield the appropriate volume fraction *m*, and is discretised using triangular elements. The number of elements varies from 300,000 to 500,000. The unknown displacement field is interpolated using quadratic Lagrangian shape functions. The corresponding number of degrees of freedom varies from 600,000 to 1,000,000.

The following conditions are assumed at the rod – matrix interface (Fig. 6):

(i) perfect bonding (i.e., continuity of the mechanical displacement field) and

(ii) continuity of the electric potential.

Moreover, periodic boundary conditions are considered at the boundary of the square representative unit cell 'RSFC rod – polymer matrix'. The matrix of effective electromechanical constants of the composite is computed column-wise, performing calculations for the average strain and electric fields imposed on the composite structure. The Geometric Multigrid[67] iterative solver (V-cycle, successive over-relaxation pre- and post-smoother, direct coarse solver) is employed. After solving the electroelastic equilibrium problem, the effective electromechanical constants of the 1–3-type composite are computed, by averaging the resulting local stress and electric-displacement fields over the representative unit cell.

Examples of the volume-fraction dependence of the effective parameters of the 1–3-type composites (Fig. 7 and Table 6) suggest that the auxetic polymer component strongly influences the piezoelectric properties irrespective of the piezoelectric activity of the RFSC component. The negative Poisson's ratio of the polymer matrix that surrounds the RFSC rods (Fig. 6) leads to changes in sgn d_{31}^*, sgn g_{31}^* and sgn k_{31}^*. As a consequence, conditions (10) and

$$d_{33}^* / |d_{31}^*| >> 1 \text{ and } k_{33}^* / |k_{31}^*| >> 1 \qquad (11)$$

are valid in the wide *m* ranges. The large values of $d_{33}^* \sim 10^3$ pC / N at the valid conditions (10) and (11) make the composites of interest for actuator and energy-harvesting applications. Moreover, values of $g_{33}^* > 100$ mV·m / N and $g_h^* > 100$ mV·m / N are also achieved in wide *m* ranges irrespective of the RFSC component (see Table 6 and Fig. 7), and this performance is of value for sensor applications. Large values of max g_{33}^* and max g_h^* at $0 < m < 0.01$ are a result of the strong influence of the dielectric and elastic properties of the polymer component on the electromechanical properties of the composite. Moreover, the influence of the elastic properties of the polymer component remains significant at $m < 0.5$ and leads, for example, to large values of d_h^* (curve 1 in Fig. 7a) and k_h^* (curve 1 in Fig. 7b). On comparing data on the piezoelectric properties from Fig. 7 and Table 6, good agreement is observed between results obtained by means of the matrix method and FEM in a wide *m* range.

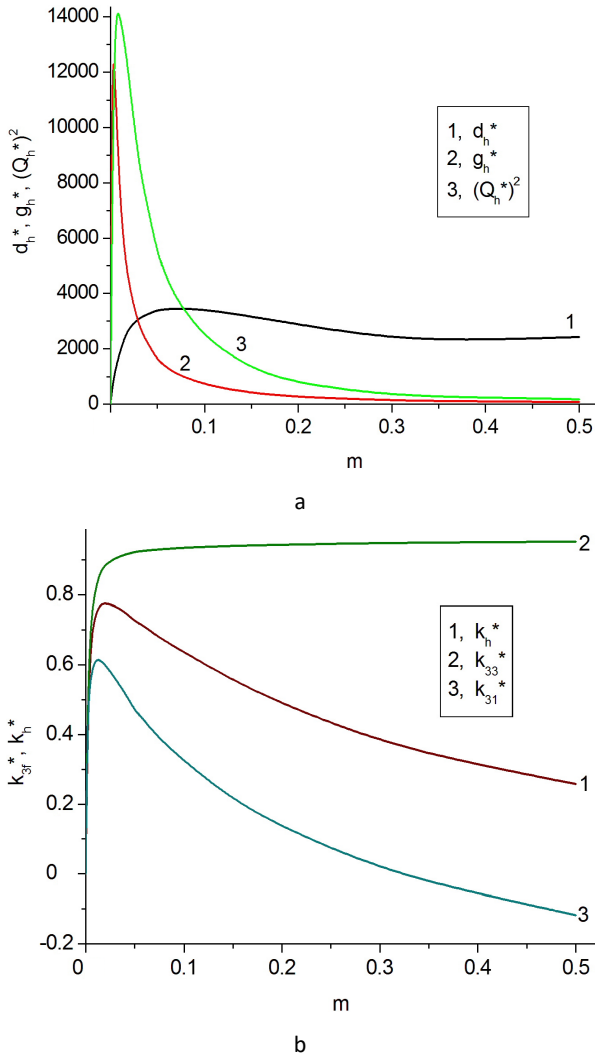

Fig. 7. Effective parameters of the 1–3-type PMN–0.33PT RFSC / auxetic polyethylene composite: (a) hydrostatic piezoelectric coefficients d_h^* (in pC / N) and g_h^* (in mV m / N), and squared hydrostatic figure of merit $(Q_h^*)^2$ (in 10^{-12} Pa^{-1}) and (b) electromechanical coupling factors k_{3f}^* and k_h^*. The schematic of the composite is shown in Fig. 6, and the effective parameters have been calculated by means of the matrix method.

The RFSC component with the largest $d_h^{(1)}$ value (in our case PMN–0.33PT with $d_h^{(1)} = 160$ pC / N) leads to the largest values of d_h^*, g_h^*, $(Q_h^*)^2$ (see Table 6), and k_h^* of the related composite. The composite system based on the PMN–0.33PT RFSC has advantages over the 1–3-type PZT ceramic / auxetic polyurethane composite: for instance, the latter composite is characterised[55] by max d_h^* = 1458 pC / N and max k_h^* = 0.567. As seen from Fig. 7, the d_h^* value of the PMN–0.33PT-based composite is approximately 2–3 times larger than the aforementioned max d_h^*, and the k_h^* is comparable to the aforementioned max k_h^*. It should be added that the large values of d_h^*, g_h^*, $(Q_h^*)^2$ and k_h^* (Table 6 and Fig. 7) are important for hydroacoustic applications of the studied 1–3-type composites.

Table 6. Volume-fraction dependences of piezoelectric coefficients d_{31}^*, d_{33}^* and d_h^* (in pC /N), g_{31}^*, g_{33}^* and g_h^* (in mV·m / N), and squared figures of merit $(Q_{33}^*)^2$ and $(Q_h^*)^2$ (in 10^{-12} Pa^{-1}) of 1–3-type composites based on [001]-poled RFSCs, FEM calculations

m	d_{31}^*	d_{33}^*	d_h^*	g_{31}^*	g_{33}^*	g_h^*	$(Q_{33}^*)^2$	$(Q_h^*)^2$
PMN–0.28PT / auxetic polyethylene								
0.01	517	664	1700	1590	2040	5220	1350	8840
0.03	608	887	2100	523	763	1810	677	3800
0.05	576	955	2110	282	468	1030	447	2170
0.07	523	992	2040	178	338	694	335	1420
0.10	438	1030	1910	102	239	44.4	246	842
0.15	305	1060	1670	46.0	160	252	170	421
0.20	190	1080	1460	21.2	120	162	130	237
0.30	5.11	1110	1120	0.371	80.5	81.2	89.4	90.9
0.50	–244	1150	662	–10.3	48.8	28.1	56.1	18.6
0.70	–406	1170	358	–12.1	34.9	10.7	40.8	3.83
0.90	–523	1180	133	–12.0	27.1	3.1	32.0	2.41
PMN–0.33PT / auxetic polyethylene								
0.01	592	758	1940	2280	2920	7480	2210	14500
0.03	894	1300	3090	800	1160	2760	1510	8530
0.05	929	1530	3390	437	720	1590	1100	5390
0.07	892	1670	3450	278	521	1080	870	3730
0.10	789	1820	3400	161	371	693	675	2360
0.15	587	1980	3150	74.0	250	398	495	1250
0.20	387	2100	2870	34.7	189	258	397	740
0.30	31.1	2280	2340	1.73	127	130	290	304
0.50	–51.2	2520	2420	–1.57	77.1	74.0	194	179
0.70	–904	2670	862	–18.7	55.3	17.9	148	15.4
0.90	–1210	2780	360	–18.8	43.1	5.5	120	1980
PZN–0.08PT / auxetic polyethylene								
0.01	531	681	1740	2140	2740	7020	1870	12200
0.03	820	1200	2840	803	1180	2790	1420	7920
0.05	859	1430	3148	446	742	1630	1060	5130
0.07	827	1580	3230	285	545	1120	861	3620
0.10	731	1730	3190	164	389	720	673	2300
0.15	537	1900	2970	74.6	264	268	410	729
0.20	340	2040	2720	33.6	201	258	410	729
0.30	–16.4	2240	2210	–0.999	136	134	305	296
0.50	–576	2510	1360	–19.1	83.2	45.0	209	61.2
0.70	–992	2700	716	–22.1	60.1	15.9	162	11.4
0.90	–1320	2830	190	–21.9	46.9	3.1	133	0.589

Piezoelectric performance of 1–3-type composites with porous polymer matrices

Now we assume that the 1–3-type composite contains a system of parallelepipedic RFSC rods in a porous polymer matrix (Fig. 8). The RFSC rods have a square base and characterised by a periodical square arrangement in the (X_1OX_2) plane. The main crystallographic axes X, Y, and Z of the RFSC rod are parallel to the following co-ordinate axes: X || OX_1, Y || OX_2 and Z || OX_3, and the spontaneous polarisation vector is $\boldsymbol{P}_s^{(1)} \uparrow\uparrow OX_3$, i.e., we consider a case of the [001]-poled RFSC component. The porous polymer matrix that surrounds the RFSC rods (Fig. 8) contains a system of spheroidal air inclusions (pores) that are described by the equation[61]

$$(x_1 / a_1)^2 + (x_2 / a_1)^2 + (x_3 / a_3)^2 = 1 \quad (12)$$

relative to the axes of the rectangular co-ordinate system ($X_1X_2X_3$), and semiaxes of the spheroid from Eq. (12) equal a_1, $a_2 = a_1$ and a_3 (see inset in Fig. 8). The porous matrix is characterised by 3–0 connectivity. It is assumed that the pores are regularly distributed in the polymer matrix and occupy sites of a simple tetragonal lattice. The shape of each pore is characterised by an aspect ratio $\rho_p = a_1 / a_3$ that is fixed over the composite sample. The radius or the largest semiaxis of each pore (e.g., $a_1 = a_2$ for the oblate pore) remains considerably less than the length of the side of the square being the intersection of the rod by the (X_1OX_2) plane. The RFSC / porous polymer composite (Fig. 8) is characterised[61] by 1–3–0 connectivity.

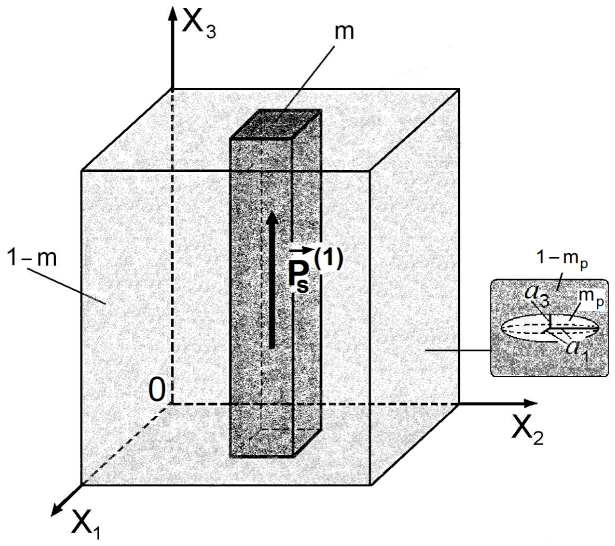

Fig. 8. Schematic of the 1–3–0 RFSC / porous polymer composite. ($X_1X_2X_3$) is the rectangular co-ordinate system concerned with the composite sample. m and $1 - m$ are volume fractions of the RFSC and porous polymer, respectively, m_p is the volume fraction of air in the porous polymer matrix. $\boldsymbol{P_s}^{(1)}$ is the spontaneous polarisation vector of the RFSC rod. In the inset a spheroidal pore with semiaxes a_f is shown schematically (reprinted from Topolov, Krivoruchko and Bisegna,[61] with permission from Elsevier, www.elsevier.com).

The effective electromechanical properties of the 1–3–0 composite are evaluated as follows. At the first stage the effective properties of the polymer matrix with aligned spheroidal pores are determined[61] as a function of the volume fraction of the pores (or porosity of the polymer matrix) m_p and the aspect ratio ρ_p. The corresponding calculation is based on Eshelby's concept of spheroidal inclusions in heterogeneous solids.[68] The effective properties of the 3–0 porous polymer are represented[61, 69] as follows:

$$|| C^{(3\text{-}0)} || = || C^{(pol)} ||\cdot[|| I || - m_p(|| I || - (1 - m_p)|| S ||)^{-1}]. \quad (13)$$

In Eq. (13) $|| C^{(pol)} ||$ is the 9×9 matrix of the electromechanical properties of the polymer component, $|| I ||$ is 9×9 identity matrix, and $|| S ||$ is the 9×9 matrix that comprises components of the electroelastic Eshelby tensor. The components of $|| S ||$ depend[68] on the aspect ratio ρ_p of the pore and on the properties of the polymer component. The $|| C^{(pol)} ||$ matrix from Eq. (13) is represented in the general form[9, 10, 61, 69] as follows:

$$|| C^{(pol)} || = \begin{pmatrix} || c^{(pol),E} || & || e^{(pol)} ||^{t} \\ || e^{(pol)} || & -|| \varepsilon^{(pol),\xi} || \end{pmatrix}. \quad (14)$$

In Eq. (14) $|| c^{(pol),E} ||$ is the 6×6 matrix of elastic moduli at E = const, $|| e^{(pol)} ||$ is the 3×6 matrix of the piezoelectric coefficients, $|| \varepsilon^{(pol),\xi} ||$ is the 3×3 matrix of dielectric permittivities at ξ = const, and superscript "t" refers to the transposed matrix. The $|| C^{(3\text{-}0)} ||$ matrix from Eq. (13) has the structure similar to that shown in Eq. (14). In the present study we consider piezo-passive polymers (see Table 3), and therefore, all the elements of $|| e^{(pol)} ||$ equal zero. At the second stage we evaluate the effective electromechanical properties of the 1–3–0 composite (Fig. 8) by means of the matrix method.[10, 61] The effective properties and related parameters of the studied composite depend on the volume fraction of the RFSC m, porosity of the surrounding matrix m_p and the aspect ratio ρ_p of the pore.

The studied 1–3–0 composite is of interest due to the large values of the piezoelectric coefficient d_{33}^* (Fig. 9a) and anisotropy factors $\zeta_{d3j} = d_{33}^* / d_{31}^*$ (Fig. 9b) and $\zeta_{k3j} = k_{33}^* / k_{31}^*$ (Fig. 9c). The formation of oblate pores in the polymer medium (see inset in Fig. 8) leads to a large difference between the elastic moduli $c_{11}^{(pol)}$ and $c_{33}^{(pol)}$ of the porous polymer and leads to a pronounced piezoelectric effect along the poling axis OX_3. On increasing the porosity m_p with an aspect ratio ρ_p = const or with increasing ρ_p at m_p = const, the piezoelectric coefficient of the composite d_{33}^* increases at m = const (Fig. 9a). The formation of oblate pores leads to a large anisotropy of d_{3j}^* (Fig. 9b) and k_{3j}^* (Fig. 9c). The curves 4–6 in Figs. 9b and 9c suggest that conditions (11) are valid in some m ranges. This is due to the considerable weakening of the lateral piezoelectric effect in the composite sample (Fig. 8) wherein the pores are oriented almost parallel to the (X_1OX_2) plane. In comparison to $\min\zeta_{d3j}$, values of $\min\zeta_{k3j}$ are more sensitive to changes in porosity m_p (cf. Figs. 9b and 9c), and a non-monotonic character of curves of ζ_{k3j} is observed at changes in m_p (see curves 4–6 in Fig. 9, c). This is accounted for by the role of elastic compliances s_{jj}^{*E} in forming the electromechanical coupling. Based on Eq. (8), we represent the anisotropy factor ζ_{k3j} as

$$\zeta_{k3j} = \zeta_{d3j}(s_{11}^{*E} / s_{33}^{*E})^{1/2}. \quad (15)$$

Eq. (15) means that the anisotropy of the electromechanical coupling in the studied 1–3–0 composite strongly depends on the elastic anisotropy that depends on the orientation of pores and their volume fraction in the polymer medium.

The performance of the 1–3–0 composite has obvious advantages over conventional ferroelectric $PbTiO_3$-type ceramics with a large piezoelectric anisotropy.[70, 71] For instance, at the volume fraction of the RFSC component $m \approx 0.1$, the piezoelectric coefficient of the composite d_{33}^* (Fig. 9a) is about 20–40 times larger than the piezoelectric coefficient d_{33} of the $PbTiO_3$-type ceramics,[70] and conditions (11) are valid (Figs. 9b and 9c). The strong and highly anisotropic electromechanical coupling in the 1–3–0 composite is due to the combination of the properties of the RFSC and the porous polymer matrix at $\rho_p >> 1$. The aforementioned advantages of the studied 1–3–0 composite are of value for transducer, acoustic, sensor, and energy-harvesting applications.

Piezoelectric performance of 1–3-type composites with laminar polymer matrices

The three-component composite structures consisting of ferroelectric ceramic rods and polymer layers were first studied by Topolov and Turik.[72,73] The large piezoelectric anisotropy, the non-monotonic dependence of a series of the piezoelectric coefficients on volume concentration of the piezo-active component and the large figures of merit[72,73] become attractive factors for further piezotechnical applications. The performance of the three-component composite based on the [001]-poled PMN–0.33PT RFSC was first discussed in Ref. 74. Now we consider two effects. The first effect is concerned with elastic properties of a laminar polymer

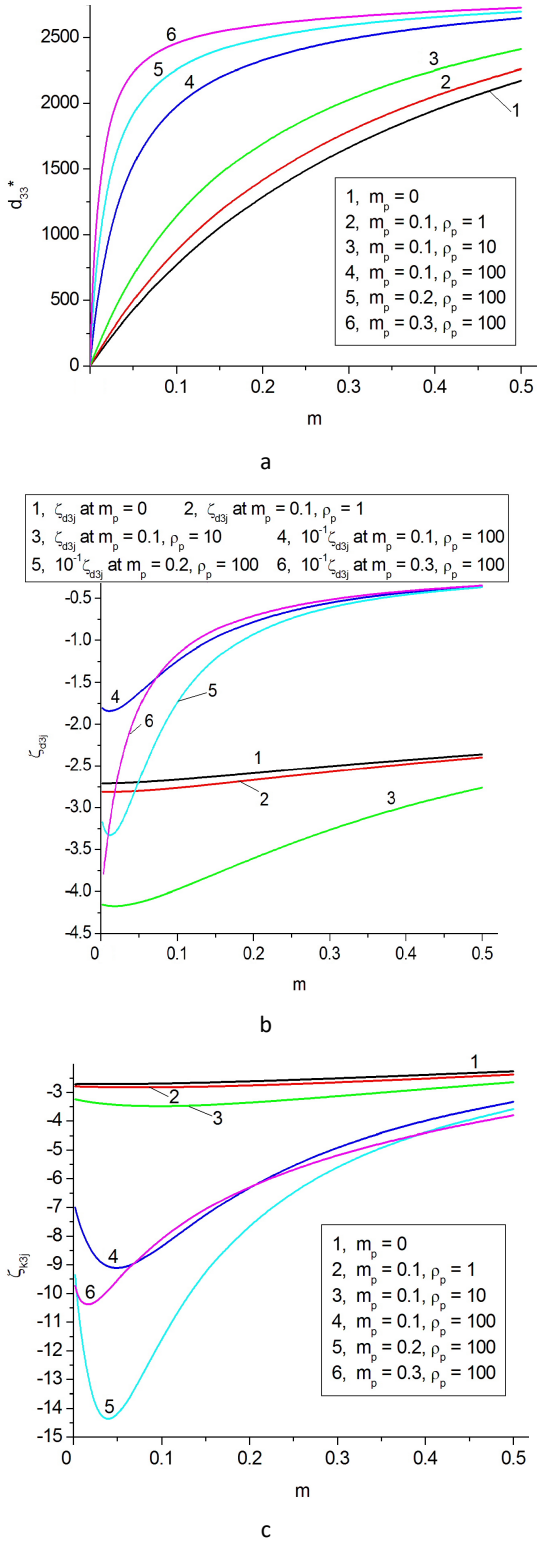

Fig. 9. Piezoelectric coefficient d_{33}^* (a, in pC / N) and anisotropy factors ζ_{d3j} (b) and ζ_{k3j} (c) of the 1–3 PMN–0.33PT RFSC / polyurethane composite (m_p = 0, curves 1) and 1–3–0 PMN–0.33PT RFSC / porous polyurethane composite (curves 2–6). The schematics of the 1–3 and 1–3–0 composites are shown in Fig. 6 and Fig. 8, respectively.

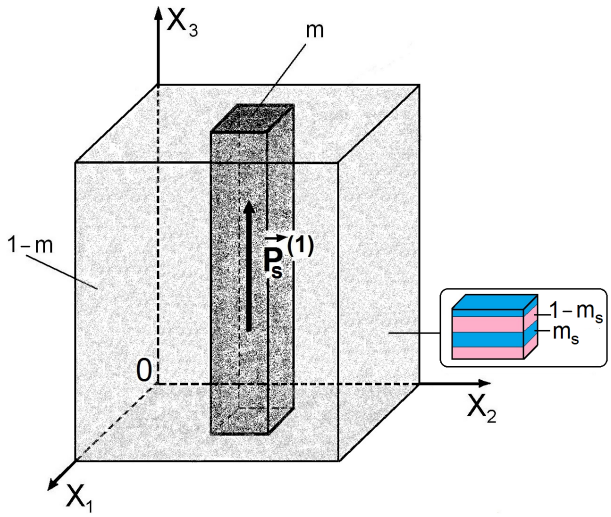

Fig. 10. Schematic of the 1–2–2 RFSC / polymer-1 / polymer-2 composite. ($X_1X_2X_3$) is the rectangular co-ordinate system concerned with the composite sample. m and $1 - m$ are volume fractions of the RFSC and laminar polymer matrix, respectively, and m_s is the volume fraction of the polymer component with the larger stiffness in the laminar matrix. $\boldsymbol{P_s^{(1)}}$ is the spontaneous polarisation vector of the RFSC rod.

matrix on the performance of the 1–3-type composite based on the PMN–0.33PT RFSC.

It is assumed that the RFSC rods are regularly distributed in the large laminar polymer matrix (Fig. 10), and the composite is characterised by 1–2–2 connectivity. A square arrangement of the rods is observed in the (X_1OX_2) plane, and its main crystallographic axes are oriented as follows: X || OX_1, Y || OX_2 and Z || OX_3. The layers of the two polymers are regularly distributed along the OX_3 axis (see inset in Fig. 10) that is the poling axis of the composite sample as a whole. To analyse the effective properties and related parameters of the 1–2–2 composite, we first evaluate the properties of the laminar polymer matrix (2–2 connectivity, matrix method) and then the properties of the system "rods – laminar matrix" (1–3 connectivity, either matrix method or FEM).

Data from Table 7 show that the combination of the polymer layers with the larger difference between elastic moduli (e.g., araldite and polyurethane, see Table 3) influences the lateral piezoelectric effect to a larger degree. The role of the laminar matrix is similar to the role of the system of the highly oblate pores in the 1–3–0 composite. The influence of the laminar matrix on the longitudinal piezoelectric effect is almost unchanged when substituting the araldite layers with the polyurethane ones (see d_{33}^*, g_{33}^* and k_{33}^* in Table 7). The graphs in Figs. 11a and 11b show that absolute max d_h^* of the composites with different laminar matrices are achieved almost in the same m and m_s ranges, however values of d_h^* are larger in the case of the composite with the araldite/polyethylene matrix. As a consequence, the larger absolute max k_h^* is achieved (Fig. 11c) in the composite with the araldite/polyethylene matrix. We see that the values of absolute max d_h^* and absolute max k_h^* (Fig. 11) are smaller than those in the related 1–3-type composite with the auxetic polyethylene matrix

Table 7. Effective piezoelectric coefficients d_{31}^*, d_{33}^* (in pC /N), g_{31}^*, g_{33}^* (in mV·m / N) and electromechanical coupling factor k_{33}^* of 1–2–2 composites based on the [001]-poled PMN–0.33PT RFSC (schematic of the 1–2–2 composite is shown in Fig. 10)

m_s	m	d_{31}^* [a]	d_{33}^* [a]	g_{33}^* [a]	k_{33}^* [a]	d_{31}^* [b]	d_{33}^* [b]	g_{33}^* [b]	k_{33}^* [b]
PMN–0.33PT / araldite / polyethylene (m_s is the volume fraction of araldite in the laminar matrix)									
0.10	0.15	–394	1820	247	0.935	–397	1820	247	0.935
	0.20	–484	2030	188	0.941	–486	2030	188	0.941
	0.25	–562	2180	152	0.945	–565	2180	152	0.945
0.15	0.15	–369	1780	246	0.934	–371	1780	246	0.934
	0.20	–454	1990	188	0.940	–458	1990	187	0.940
	0.25	–536	2150	151	0.944	–538	2140	151	0.944
0.20	0.15	–349	1750	246	0.932	–352	1740	246	0.932
	0.20	–436	1960	187	0.939	–438	1950	187	0.939
	0.25	–517	2120	151	0.943	–518	2120	151	0.943
0.25	0.15	–334	1710	245	0.931	–337	1710	245	0.931
	0.20	–420	1920	186	0.938	–423	1920	186	0.938
	0.25	–499	2080	151	0.943	–502	2080	151	0.943
PMN–0.33PT / polyurethane / polyethylene (m_s is the volume fraction of polyurethane in the laminar matrix)									
0.10	0.15	–453	1850	248	0.936	–456	1850	248	0.936
	0.20	–543	2060	188	0.942	–546	2050	188	0.942
	0.25	–623	2200	152	0,946	–625	2200	152	0,946
0.15	0.15	–439	1820	247	0,935	–442	1820	247	0,935
	0.20	–528	2030	188	0,941	–531	2030	188	0,941
	0.25	–607	2180	151	0,945	–610	2180	152	0,945
0.20	0.15	–428	1790	247	0,934	–431	1790	247	0,934
	0.20	–517	2000	188	0.941	–520	2000	188	0.940
	0.25	–597	2160	151	0,945	–599	2160	151	0,945
0.30	0.15	–412	1730	245	0.932	–415	1730	245	0.932
	0.20	–501	1950	187	0,939	–504	1950	187	0,939
	0.25	–580	2110	151	0.943	–583	2110	151	0.943

[a] Calculated by means of the matrix method for the 1–3-type composite structure

[b] Calculated by means of FEM for the 1–3-type composite structure

(see Fig. 7). Such a performance is related to the elastic properties of the matrix surrounding the RFSC rods. The auxetic polyethylene matrix is more compliant, and its Poisson's ratio is negative. In contrast to this, the laminar matrix is characterised by the larger elastic moduli and positive Poisson's ratio. As follows from Table 7, good agreement between the parameters evaluated for the system "rods – laminar matrix" by using two different methods is achieved.

Now we assume, that instead of the RFSCs rods in the form of the rectangular parallelepiped, the 1–2–2 composite consists of a system of cylindrical rods with a circular base. The centres of symmetry of their bases form a simple square lattice in the (X_1OX_2) plane. The main crystallographic axes of each rod are oriented as follows: X || OX_1, Y || OX_2 and Z || OX_3. We compare a set of effective parameters of the related 1–2–2 composites in a wide m range (Table 8). It is seen that the shape of the rod influences the lateral piezoelectric effect and hydrostatic parameters of the composite, although this influence is not large. In our opinion, such an influence is due to the relatively large difference between elastic moduli of the RFSC and laminar matrix. The large values of d_h^*, k_h^*, g_{33}^*, and other parameters of the studied 1–2–2 composites are to be taken into account in hydroacoustic, piezoelectric sensor, energy-harvesting, and related applications.

Conclusions

We have highlighted the effective electromechanical properties and related parameters of piezo-active composites based on the domain-engineered relaxor-ferroelectric single crystals with the perovskite-type structure. Among the RFSCs with remarkable electromechanical properties, of interest are PMN–xPT and PZN–xPT, especially poled along either [001] or [011] in the perovskite unit cell. These RFSCs can be used as main components in the composites of the 2–2 and 1–3 types. Our main research results are concluded as follows.

(i) Examples of the polarisation orientation effect in the 2–2-type composites show that this effect is of value to significantly improve the hydrostatic piezoelectric response. The rotation of the main crystallographic axes of the [011]-poled RFSC around the poling axis leads to large values of the hydrostatic parameters d_h^*, g_h^* and $(Q_h^*)^2$. An additional opportunity to increase $(Q_h^*)^2$ and to reach a larger anisotropy of squared figures of merit $(Q_{3j}^*)^2$ involves replacing the monolithic polymer component with an auxetic polymer. Condition (10) for the large anisotropy of $(Q_{3j}^*)^2$ in 2–2-type composite is due to an polarisation orientation effect, high

Table 8. Effective piezoelectric coefficients d_{31}^*, d_{33}^*, d_h^* (in pC / N), g_{33}^* and g_h^* (in mV·m / N)[a] of the 1–2–2 PMN–0.33PT / araldite / polyethylene composite

m	0.03	0.05	0.10	0.15	0.20	0.30	0.50	0.70
SC rods in the form of the rectangular parallelepiped with the square base, volume fraction of araldite in the laminar matrix m_s = 0.15								
d_{31}^*	–101	–156	–273	–371	–458	–612	–865	–1070
d_{33}^*	667	970	1470	1780	1990	2260	2540	2690
g_{33}^*	988	661	359	246	187	127	77.0	55.3
d_h^*	465	658	924	1040	1070	1040	810	550
g_h^*	689	448	226	144	101	58.4	24.6	11.3
SC rods in the form of the circular cylinder, volume fraction of araldite in the laminar matrix m_s = 0.15								
d_{31}^*	–100	–155	–271	–367	–453	–604	–862	–1100
d_{33}^*	667	971	1470	1790	1990	2260	2540	2690
g_{33}^*	988	661	359	246	188	127	77.0	55.3
d_h^*	467	661	928	1050	1080	1050	816	490
g_h^*	692	450	227	145	102	59.0	24.7	10.1
SC rods in the form of the rectangular parallelepiped with the square base, volume fraction of araldite in the laminar matrix m_s = 0.20								
d_{31}^*	–92.1	–144	–256	–352	–438	–592	–849	–1060
d_{33}^*	639	935	1430	1740	1950	2230	2520	2680
g_{33}^*	975	655	358	246	187	127	77.0	55.3
d_h^*	455	647	918	1040	1070	1050	822	560
g_h^*	694	453	230	147	103	59.8	25.1	11.6
SC rods in the form of the circular cylinder, volume fraction of araldite in the laminar matrix m_s = 0.20								
d_{31}^*	–91.7	–143	–254	–348	–433	–585	–847	–1090
d_{33}^*	640	936	1430	1750	1960	2230	2530	2670
g_{33}^*	975	655	358	246	187	127	77.0	55.3
d_h^*	457	650	922	1050	1090	1060	836	490
g_h^*	696	455	231	148	104	60.4	25.4	10.1

[a] Calculated by means of the matrix method (2–2 laminar matrix) and by means of FEM (1–3-type composite structure)

piezoelectric activity of the RFSC and the elastic properties of the components.

(ii) In the 1–3-type composites we use the [001]-poled RFSC rods and modify the polymer matrix surrounding the rods. We consider cases of the monolithic, auxetic, porous and laminar polymer matrices. In each case of modifying the matrix, we see the advantages of the studied 1–3-type composite over the known piezoelectric materials. This modification leads to appreciable changes in the elastic properties of the matrix, and these changes strongly influence the lateral piezoelectric effect and hydrostatic parameters of the composite. Examples of validity of conditions (11) show that the 1–3-type composites are of value as materials that combine the high piezoelectric activity and large piezoelectric anisotropy. These composites are also of interest due to the large hydrostatic parameters and electromechanical coupling factors.

(iii) Comparing data on the related 1–3- and 2–2-type composites, we state that 1–3 connectivity provides additional advantages due to opportunities to modify the polymer matrix and its properties for improving the effective parameters of the composite.

(iv) A comparison of the effective parameters evaluated for some 1–3-type composites by means of different methods shows that good agreement is achieved in a wide volume-fraction (m) range irrespective of the properties and microgeometry of the polymer matrix.

Finally, knowledge of the piezoelectric coefficients, electromechanical coupling factors and figures of merit is of benefit for design of advanced RFSC-based composites as energy-harvesting materials with preferable directions for the conversion and propagation of energy along specific directions.

Acknowledgements

The authors would like to thank Prof. Dr. A. E. Panich, Prof. Dr. I. A. Parinov, Prof. Dr. A. A. Nesterov, and Prof. Dr. V. P. Sakhnenko (Southern Federal University, Rostov-on-Don, Russia) for their continuing interest in the research problems. Prof. Dr. C. R. Bowen would like to acknowledge funding from the European Research Council under the European Union's Seventh Framework Programme (FP/2007-2013) / ERC Grant Agreement no. 320963 on Novel Energy Materials, Engineering Science and Integrated Systems (NEMESIS). In the present paper the results on the research work No. 1597 have been represented within the framework of the base part of the state task No. 2014/174 in the scientific activity area at the Southern Federal University (Russia).

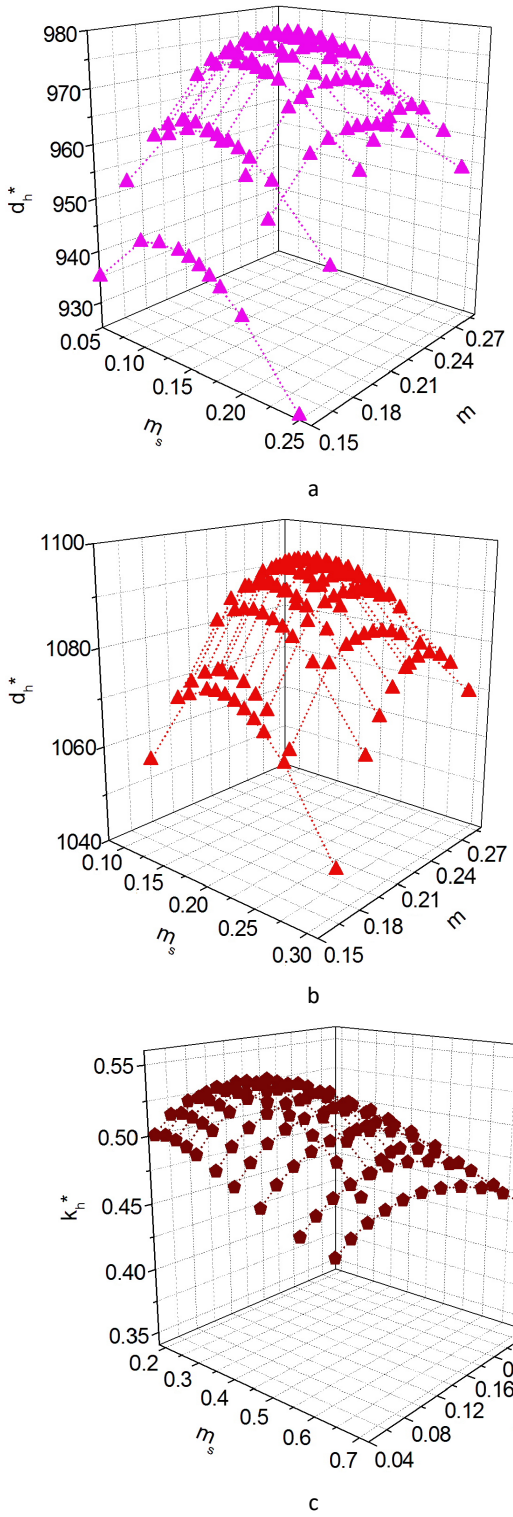

Fig. 11. Hydrostatic piezoelectric coefficient d_h^* (a and b, in pC / N) and hydrostatic electromechanical coupling factor k_h^* (c) of the 1–2–2 PMN–0.33PT RFSC / polyurethane / polyethylene composite (a) and 1–2–2 PMN–0.33PT RFSC / araldite / polyethylene composite (b and c). In graph a, m_s is the volume fraction of polyurethane in the laminar matrix. In graphs b and c, m_s is the volume fraction of araldite in the laminar matrix.

Notes and references

1 S.-E. Park and T. R. Shrout, *Mater. Res. Innov.*, 1997, **1**, 20.

2 L. E. Cross, Piezoelectricity. Evolution and Future of a Technology, Eds. W. Heywang, K. Lubitz, and W. Wersing (Springer, Berlin, Heidelberg, 2008), 131.

3 S. Zhang and F. Li, *J. Appl. Phys.*, 2012, **111**, 031301.

4 S. Zhang, F. Li, J. Luo, R. Sahul, and T. R. Shrout, *IEEE Trans. Ultrason., Ferroelec., a. Freq. Contr.*, 2013, **60**, 1572.

5 T. Ritter, X. Geng, K. K. Shung, P. D. Lopath, S.-E. Park, and T. R. Shrout, *IEEE Trans. Ultrason., Ferroelec., a. Freq. Contr.*, 2000, **47**, 792.

6 K. C. Cheng, H.L.W. Chan, C.L. Choy, Q. Yin, H. Luo, and Z. Yin, *IEEE Trans. Ultrason., Ferroelec., a. Freq. Contr.*, 2003, **50**, 1177.

7 K. Ren, Y. Liu, X. Geng, H. F. Hofmann, and Q. M. Zhang, *IEEE Trans. Ultrason., Ferroelec., a. Freq. Contr.*, 2006, **53**, 631.

8 W. Wang, C. He, and Y. Tang, *Mater. Chem. Phys.*, 2007, **105**, 273.

9 V. Yu. Topolov and C. R. Bowen, Electromechanical Properties in Composites Based on Ferroelectrics (Springer, London, 2009).

10 V. Yu. Topolov, P. Bisegna, and C. R. Bowen, Piezo-active Composites. Orientation Effects and Anisotropy Factors (Springer, Berlin, Heidelberg, 2014).

11 V. Yu. Topolov, C. R. Bowen, and P. Bisegna, Advanced Materials. Manufacturing, Physics, Mechanics and Applications, Eds. I. A. Parinov, S.-H. Chang, and V. Yu. Topolov (Springer, Cham, Heidelberg, New York, Dordrecht, London, 2016), 179.

12 I. S. Zheludev, Physics of Crystalline Dielectrics, Vols. 1 and 2 (Plenum: New York, 1971).

13 T. Ikeda, Fundamentals of Piezoelectricity (Oxford University Press, Oxford, New York, Toronto, 1990).

14 Y. Xu, Ferroelectric Materials and Their Applications (North-Holland, Amsterdam, London, New York, Toronto, 1991).

15 B. Jaffe, W. R. Cook, and H. Jaffe, Piezoelectric Ceramics (Academic Press, London, New York, 1971).

16 G. Helke and K. Lubitz, Piezoelectricity. Evolution and Future of a Technology, Eds. W. Heywang, K. Lubitz, and W. Wersing (Springer, Berlin, Heidelberg, 2008), 89.

17 J. R. White, B. De Poumeyrol, J. M. Hale, and R. Stephenson, *J. Matser. Sci.*, 2004, **39**, 3105.

18 X. Li and Y. Zhang, *J. Intell. Mater. Syst. Struct.*, 2010, 21, 1213.

19 Z. Yang, D. Zeng, H. Wang, C. Zhao, and J. Tan, *Smart Mater. Struct.*, 2015, **24**, 075029.

20 E. K. Akdogan, M. Allahverdi, and A. Safari, *IEEE Trans. Ultrason., Ferroelec., a. Freq. Contr.*, 2005, **52**, 746.

21 S.-E. Park and T. R. Shrout, *J. Appl. Phys.*, 1997, **82**, 1804.

22 S.-E. Park and W. Hackenberger, *Curr. Opin. Solid State Mater. Sci.*, 2000, **6**, 11.

23 H. Fu and R. E. Cohen, *Nature*, 2000, **403**, 281.

24 M. Davis, *J. Electrocer.*, 2007, **19**, 23.

25 X. Huo, S. Zhang, G. Liu, R. Zhang, J. Luo, R. Sahul, W. Cao, and T. R. Shrout, *J. Appl. Phys.*, 2013, **113**, 074106.

26 X. Liu, S. Zhang, J. Luo, T. R. Shrout, and W. Cao, *J. Appl. Phys.*, 2009, **106**, 074112.

27 C. He, X. Li, Z. Wang, Y. Liu, D. Shen, T. Lia, and X. Long, *CrystEngComm*, 2012, **14**, 4513.

28 L. Zheng, X. Yi, S. Zhang, W. Jiang, B. Yang, R. Zhang, and W. Cao, *Appl. Phys. Lett*., 2013, **103**, 122905.
29 J. Erhart and W. Cao, *Ferroelectrics*, 2012, **426**, 13.
30 B. Noheda, *Curr. Opin. Solid State Mater. Sci.*, 2002, **6**, 27.
31 V. Yu. Topolov and A. V. Turik, *J. Phys.: Condens. Matter*, 2001, **13**, L771.
32 V. Yu. Topolov and A. V. Turik, *Solid State Phys*., 2002, **44**, 1355.
33 V. Yu. Topolov, Heterogeneous Ferroelectric Solid Solutions. Phases and Domain States (Springer, Berlin, Heidelberg, 2012).
34 T. Liu and C. S. Lynch, *Acta Mater*., 2003, **51**, 407.
35 R. Zhang, B. Jiang, and W. Cao, *J. Appl. Phys*., 2001, **90**, 3471.
36 R. Zhang, B. Jiang, W. Cao, and A. Amin, *J. Mater. Sci. Lett*., 2002, **21**, 1877.
37 R. Zhang, B. Jiang, W. Jiang, and W. Cao, *Mater. Lett*., 2003, **51**, 1305.
38 R. Zhang, B. Jiang, W. Jiang, and W. Cao, *Appl. Phys.Lett*., 2006, **89**, 242908.
39 J. Yin, B. Jiang, and W. Cao, *IEEE Trans. Ultrason., Ferroelec., a. Freq. Contr.*, 2000, **47**, 285.
40 M. Guennou, H. Dammak, and M. P. Thi, *J. Appl. Phys*., 2008, **104**, 074102.
41 E. G. Fesenko, V. G. Gavrilyachenko, and A. F. Semenchev, Domain Structure of Multiaxial Ferroelectric Crystals (Rostov University Press, Rostov-on-Don, 1990, in Russian).
42 R. Zhang, W. Jiang, B. Jiang, and W. Cao, Fundamental Physics of Ferroelectrics, Ed. R. E. Cohen (American Institute of Physics, Melville, 2002), 188.
43 S. Zhang, J. Luo, W. Hackenberger, and T. R. Shrout, *J. Appl. Phys*., 2008, **104**, 064106.
44 G. Liu, W. Jiang, J. Zhu, and W. Cao, *Appl. Phys. Lett*., 2011, **99**, 162901.
45 F. Wang, L. Luo, D. Zhou, X. Zhao, and H. Luo, *Appl. Phys. Lett*., 2007, **90**, 212903.
46 C. He, W. Jing, F. Wang, K. Zhu, and J. Qiu, *IEEE Trans. Ultrason., Ferroelec., a. Freq. Contr.*, 2011, **58**, 1127.
47 V. Yu. Topolov and C. R. Bowen, *J. Appl. Phys*., 2011, **109**, 094107.
48 R. E. Newnham, D. P. Skinner, and L. E. Cross, *Mater. Res. Bull.*, 1978, **13**, 525.
49 A. V. Krivoruchko and V. Yu. Topolov, *J. Phys. D: Appl. Phys*., 2007, **40**, 7113.
50 V. Yu. Topolov and A. V. Krivoruchko, *Smart. Mater. Struct*., 2009, **18**, 065011.
51 V. Yu. Topolov and A. V. Krivoruchko, *J. Appl. Phys*., 2009, **105**, 074105.
52 V. Yu. Topolov and S. V. Glushanin, *J. Phys. D: Appl. Phys*., 2002, **35**, 2008.
53 A. A. Grekov, S. O. Kramarov, and A. A. Kuprienko, *Mech. Compos. Mater*., 1989, **25**, 54.
54 F. Levassort, M. Lethiecq, D. Certon, and F. Patat, *IEEE Trans. Ultrason., Ferroelec., a. Freq. Contr.*, 1997, **44**, 445.
55 L. V. Gibiansky and S. Torquato, *J. Mech. Phys. Solids*, 1997, **45**, 689.
56 K. E. Evans and K. L. Alderson, *J. Mater. Sci. Lett*., 1992, **11**, 1721.
57 I. N. Groznov, Physics Encyclopaedia (Sovetskaya Entsiklopediya, Moscow, 1983, in Russian), 178.
58 A. A. Grekov, S. O. Kramarov, and A. A. Kuprienko, *Ferroelectrics*, 1987, **76**, 43.
59 C. R. Bowen and V. Yu. Topolov, *Ferroelectrics*, 2014, **466**, 21.
60 S. V. Bezus, V. Yu. Topolov, and C. R. Bowen, *J. Phys. D: Appl. Phys*., 2006, **39**, 1919.
61 V. Yu. Topolov, A. V. Krivoruchko, and P. Bisegna, *Compos. Sci. Technol*., 2011, **71**, 1082.
62 V. Yu. Topolov, C. R. Bowen, P. Bisegna, and A. V. Krivoruchko, *Mater. Chem. Phys*., 2015, **151**, 187.
63 V. Yu. Topolov, C. R. Bowen, and P. Bisegna, *Sens. Actuat. A – Phys*., 2015, **229**, 94.
64 V. Yu. Topolov, C. R. Bowen, P. Bisegna, and A. E. Panich, *Funct. Mater. Lett*., 2015, **8**, 1550049.
65 V. Yu. Topolov and C. R. Bowen, *Mater. Lett*., 2015, **142**, 265.
66 COMSOL, Inc. COMSOLMultiphysics™ User's Guide (version 4.4, 2014), http://www.comsol.com.
67 W. Hacksbusch, Multi-grid Methods and Applications (Springer, Berlin, 1985).
68 J. H. Huang and S. Yu, *Compos. Eng*., 1994, **4**, 1169–1182.
69 M. L. Dunn and M. Taya, *J. Am. Ceram. Soc*., 1993, **76**, 1697.
70 S. Ikegami, I. Ueda and T. Nagata, *J. Acoust. Soc. Am*., 1971, **50**, 1060.
71 A. V. Turik and V. Yu. Topolov, *J. Phys. D: Appl. Phys*., 1997, **30**, 1541.
72 V. Yu. Topolov and A. V. Turik, *Tech. Phys. Lett*., 2001, **27**, 81.
73 V. Yu. Topolov and A. V. Turik, *Tech. Phys.*, 2001, **46**, 1093.
74 A. E. Panich, V. Yu. Topolov and S. V. Glushanin, Vibroengineering, 6th International Conference Proceedings. October 12–14, 2006. Kaunas University of Technology, Lithuania (Technologija, Kaunas, 2006), 226.